Title

Diagnostic analysis of electrodes from high-power lithium-ion cells cycled under different conditions

Journal

Journal of the Electrochemical Society, 151(6)

Authors

Striebel, Kathryn A.
Shim, Joongpyo
Cairns, Elton J.
et al.

Publication Date

2004-04-03

Diagnostic Analysis of Electrodes from High-Power Lithium-Ion Cells Cycled under Different Conditions

K.A. Striebel[a], J. Shim[a], E.J. Cairns[a], R. Kostecki[a], Y.-J. Lee[a], J. Reimer[a], T.J. Richardson[a], P.N. Ross[b], X. Song[a], G. V. Zhuang[b]

[a]Environmental Energy Technologies Division
[b]Materials Science Division
E.O. Lawrence Berkeley National Laboratory
Berkeley, CA 94720 USA

Abstract

Pouch type lithium-ion cells, with graphite and $LiNi_{0.8}Co_{0.15}Al_{0.05}O_2$, were cycled over different ranges of depth-of discharge (DOD) and at different temperatures. A combination of electrochemical, physical and chemical diagnostic evaluations, including Raman, NMR and FTIR spectroscopy, TEM, EDX, and XRD, were carried out on the components removed from the cells to form a clear picture of the mechanism for capacity and power fade in this important cell chemistry.

Both capacity fade and impedance rise were found to increase with cycling temperature and the span of the DOD. The loss of cycleable Li, most likely due to solvent reduction on the anode, was linear in cell test time and the room temperature cells showed an SEI composition and degree of graphite disorder that roughly correlated with the extent of the Li consumption. However, electrochemical analysis showed that the cathode was controlling the performance loss in the cell. TEM and NMR showed evidence of crystalline defects and degradation of the Li-Ni environment, respectively, though no major new phases were identified, in agreement with the XRD results. FTIR analysis of the cathode revealed no evidence of polymeric deposits on the cathode particles although both Raman and TEM showed evidence of P-containing deposits. Raman mapping showed a noticeable change of the active material/carbon surface concentration ratio for the cathode cycled 1000 times at 100% DOD as compared with that cycled to 70% DOD.

Key words: Lithium ion battery, diagnostics, Raman, FTIR, TEM, NMR
*Corresponding author; kastriebel@lbl.gov (K.A. Striebel)

Introduction

Lithium ion batteries are being seriously considered for application in all-electric vehicles (EV) and hybrid electric vehicles (HEV's) because of their high power and energy densities [1-2]. The class of oxides based on $LiNiO_2$, with a variety of substitutions, are considered to be good replacements for the $LiCoO_2$ in the cathode of consumer-size Li-ion cells because of it's higher specific energy and lower cost. Substitutions of part of the Ni with Co and Al improve the stability and safety characteristics of this material. The particular composition, $LiNi_{0.8}Co_{0.15}Al_{0.05}O_2$, was chosen for the cathode-active material in a large study by the DOE Advanced Technology Development (ATD) project, as their Generation 2 cell chemistry, together with an anode based on Hitachi's Mag-10 synthetic graphite. The aim of the ATD program is to develop a complete understanding of the power fade of a single cell chemistry in the HEV application and to develop predictive models for the accelerated life behavior based on these mechanisms. For this purpose, this cell chemistry has been subjected to variable temperature calendar life studies and lifecycle testing with an pulse-type profile over a very limited range of state-of-charge (SOC) [3]. Many cells have been examined to determine the mechanisms for capacity and power fade, with a wide range of diagnostic techniques, developed and refined during studies of the ATD Gen 1 cells [4,5]. The concurrence of several analytic techniques is required to understand the myriad phenomena existing in a rechargeable lithium-ion battery.

During both the calendar-life and the pulse profile testing, with the 25kW Power Assist Lifecycle profile developed by PNGV [6], the ATD cells are maintained within a very narrow range of state-of-charge (SOC) (within about ± 5% of their target of 60% SOC), except during the periodic reference performance tests (RPT). This type of testing, while of great value to the development of an HEV battery, is quite different from the 80-100% DOD cycling required for an EV battery. In the parallel DOE project, the Batteries for Advanced Transportation Technologies (BATT) program, we are concerned with research aimed at the development of batteries materials for application in EV's, as well as HEV's, and fuel cell/EV's (FCEV). In an effort to benchmark the $LiNi_{0.8}Co_{0.15}Al_{0.05}O_2$/Mag-10 cell for the EV application and take advantage of the

knowledge base being accumulated within the ATD program with this cell, we prepared and studied 12 cm^2 pouch cells, with a chemistry very similar to that in the ATD Gen 2 18650 cells. These pouch cells were cycled over a wider ranges of SOC to more fully understand the degradation mechanisms in this important chemistry. Cells were cycled with a taper charge to 4.1 V and a discharge to either 70 or 100% DOD at room temperature or 60°C. The cycle performance for these cells as well as electrochemical diagnostics and some early diagnostics of the high-temperature cells has been reported previously [7,8]. With a wider swing in SOC during cycling, these cells were seen to loose power and capacity at a much faster rate than the ATD cells. In this paper, after a summary of the cycling results, the results of several diagnostic analyses of the cell components will be presented and analyzed. These include further electrochemical diagnostics, XRD, FTIR and Raman spectroscopy, TEM, and NMR carried out in parallel to create a clearer picture of the various capacity fade mechanisms taking place during cell cycling.

Experimental

The pouch cells were constructed from unpressed one-side coated electrodes from Quallion Corp., containing 92% Hitachi Mag-10 graphite and 8% PVdF (Kureha C) binder in the anode, and 84% $LiNi_{0.8}Co_{0.15}Al_{0.05}O_2$ (Fuji), 4% SFG6 graphite, 4% acetylene black and 8% PVdF (Kureha KF100) binder in the cathode. The electrolyte was 1M $LiPF_6$ in 1:1 ethylene carbonate (EC)/diethyl carbonate (DEC) (LP40, EM Science). Details of the cell construction were reported previously [7]. After pouch cell assembly, the cells were formed with two cycles at very slow rate (C/25). Cycle-life testing was carried out with C/2 charging to 4.1V, a taper charge at 4.1 to a minimum current of C/20 (or a maximum of 2 hours) and a C/2 discharge to either a potential limit of 3.0V, for 100% depth-of-discharge (DOD) cycling, or to a discharge limit of 0.7C, for 70% DOD cycling. The cells were allowed an open circuit rest period of 15 min. between each half-cycle. Cycling was interrupted every 80 cycles to measure cell impedance and pulse power capability with the HPPC profile [6]. One cell was cycled at 60°C with the remainder cycled at room temperature. At the end of cycling, the cells were again subjected to a C/25 cycle, ending at 3.0V(100%DOD) to determine the capacity remaining in the cell. The discharged cells

were disassembled in an Ar glovebox. Electrodes were soaked in DEC overnight and dried in the glovebox prior to sampling for the various diagnostic techniques.

XRD

Xray diffraction patterns for the cathodes were obtained using a Siemens D-5000 diffractometer in reflection mode. Lattice parameters, state of charge, and crystallite sizes were determined by whole pattern fitting.

Raman Microscopy

An integrated Raman microscope system "Labram" made by ISA Groupe Horiba was used to analyze the structure and composition of the cathodes and anodes. The excitation wavelength was supplied by an internal He-Ne (632 nm) 10 mW laser. The power of the laser beam was adjusted to 0.1 mW with neutral filters of various optical densities. The size of the laser beam at the sample was ~1.2 μm. Raman mapping of the cathode surface was carried out across a 52x75 μm area at 0.7 μm lateral resolution, using a software-controlled motorized XY stage.

FTIR Spectroscopy

The FTIR measurements were performed on a Nicolet Nexus 870 Spectrometer, equipped with a broadband Mercury-Cadmium-Telluride (MCT) detector. The spectra were acquired in the Attenuated Total Reflection (ATR) mode using a hemispherical Ge optic at a spectral resolution of 4 cm^{-1}. All spectra were obtained from a 2 mm diameter area on samples pressed against the Ge crystal. The penetration depth of the (mid)-infrared light (2000 cm^{-1}) into a medium with n = 1.5 (an optical constant typical for organic compounds) is on the order of magnitude of 400 nm [9]. The ATR-FTIR spectra were corrected for the light penetration depth as function of wavelength. A linear background correction was also performed to eliminate the sloping spectral background caused by surface roughness. Both anodes and cathodes harvested from the cycled cells were analyzed by ATR-FTIR after washing to remove the electrolyte components, as discussed above**.** The electrodes were then transferred from the glove box to the He-purged

spectrometer sample chamber without exposure to air either during sample handling or measurement.

Solid State NMR Spectroscopy

^{7}Li MAS (Magic Angle Spinning) NMR experiments were carried out at 25.50 MHz on a home built spectrometer with a Doty probe equipped with 4 mm rotors for MAS. Spectra were obtained with a rotor-synchronized Hahn echo pulse sequence (90°–τ–180°–τ–acq.). Since these experiments were performed under MAS conditions, the sequence was rotor synchronized with τ being chosen as one rotor period. A 90° pulse of 1.1 μs was used with a 1 s recycle delay. The spinning speed was 21kHz. The spectra were taken at room temperature and no attempt was made to control the temperature. All shifts were referenced to 1 M LiCl (aq.) solution, at 0 ppm.

TEM

For TEM measurements, a part of the anode was dispersed in EMC, ground lightly and then some of the particles were collected on a copper grid. Sample preparation was carried out in the inert-atmosphere glove-box and the sample was then sealed in a small bottle for transportation to the Philips CM200/FEG (field emission gun) TEM at the National Center for Electron Microscopy (NCEM) at LBNL.

Results

Summary of Cycling Results

The C/2 discharge capacities for the cells in this study are shown in Figure 1. The cycling conditions and measures of performance fade are summarized in Table 1. Low-rate capacity measurements were made before cycling (the second formation cycle) and after cycling was completed. The capacity fade during C/2 cycling is larger than the low-rate (C/25) fade since the impedance of the cell is also increasing. In these cells, the coulombic efficiency was very close to 100% for all of the testing after the first formation cycle. From

these data it is clear that the capacity of cells cycled over 100% DOD and at high-temperature fades faster than that of cells cycled at room temperature and/or a more limited capacity range. It is also clear from the recovery of capacity during C/25 cycling (compared to C/2) that impedance changes in the cell are responsible for a certain fraction of the capacity fade for all of the cells studied. A measure of the increase in cell resistance at the end of discharge (EOD) after cycling was estimated from the relaxation of the voltage after the last C/1 discharge in the RPT, compared to the same experiment in a fresh cell. This impedance includes the ohmic resistance as well as the polarization resistance from the C/1 discharge, however, the difference between low and high-rate capacity fade correlates reasonably well with this increase in cell resistance. The cell power fade, calculated from the 18s discharge pulse part of the HPPC in the RPT at 50% SOC after cycling is included in Table 1 where available. For PG13 and PG03 cells, the cells were not able to support a 5C pulse very deep into the discharge without exceeding the voltage limits.

Electrochemical Analysis of the Cathode and Anode

All of the cells were disassembled after the last C/25 discharge for electrochemical, chemical and physical diagnostics. Post-test electrochemical diagnostic studies of each electrode were carried out with 1 cm^2 electrodes at C/25 in half-cells with a Li RE and CE, as discussed previously [7,8]. The first charge for the cathode post-test reveals the amount of cycleable lithium remaining in the cell, since all of the anodes were completely discharged upon removal from the cells (E vs. Li > 2V). Comparison between the second post-test cycle on the anode and cathode with the same test on fresh (uncycled) electrodes reveals the decline in the ability of the electrode to intercalate lithium, given a fresh (and large) source of lithium. This measure of capacity fade is also listed in Table 1.

The capacity of the anodes, harvested from the 25°C-cycled cells, showed essentially identical capacity to the fresh anodes in half-cell measurements, even for the cell cycled 1000 times at 100%DOD. The differential capacity plot for the 60°C-cycled anode, which showed the largest loss of 10%, is compared to that of a fresh anode in Figure 2. The biggest change in these curves occurs in the size of the stage I intercalation peak, where the

lithium is most closely packed. This is consistent with a loss of ordering in the graphite. As suggested above, the amount of lithium remaining in the cell can be determined from the charge capacity of the cathode sample removed from the cell. The difference between the original Li content and that remaining in the cell will be equal the loss of Li during cycling, due to a combination of side-reaction, isolation within the cathode or conversion to a non-active phase. The fraction of this loss consumed by side-reaction can be estimated, as shown in Figure 3, as the difference between the capacity of the cathode when supplied with an excess of Li and that remaining in the cathode. The side-reaction is usually thought to be the continual reaction between electrolyte components and the lithiated anode in an unstable SEI layer. The amount of lithium consumed in this reaction is shown in Table 4 along with various diagnostic constants to be discussed below. This calculation neglects the loss of Li during cell formation. However, the $LiNi_{0.8}Co_{0.15}Al_{0.05}O_2$ cathode shows an ICL of about 10%, comparable to the value for the Mag-10 anode. The calculations in Fig. 3 are made from the second cycle (reversible capacity of the cathode) and the ICL effect for the two electrodes is canceled out. It is interesting to plot this fade from side-reaction against the total test time for the cell, as shown in Figure 4. The rate of Li consumption through side-reaction is essentially constant for all of the cells, except possibly the 60°C cell, where acceleration of this reaction might be expected.

The build-up of the SEI layer is expected to increase the ASI of the cell and lead to power fade. However, this layer is still very conductive. Cell impedance changes such as those indicated in Table 1, if they were anode-related, should lead to significant shifts in the peak potentials in Fig. 2. This behavior was not observed and it therefore appears that most of the impedance rise in the cell is attributable to the cathode.

The electrochemical results can be summarized as follows:

- The 60°C-cell lost capacity at the highest rate (0.46%/cycle). Almost half of this loss was due to cell impedance rise (0.23%/cycle) and most of that was due to a cathode impedance rise. Only 10% of the lost capacity can be attributed to side-reaction on the anode even though a thick layer of Li_2CO_3 was detected on the anode with TEM. Previously we reported that the cathode showed a significantly increased impedance,

especially at high SOC. Impedance at EOD increased only moderately. This was attributed to an SEI film on the cathode with a SOC-dependent Li conductivity/mobility [7].

- The room temperature pouch cells cycled over 100% DOD, PG04 and PG03, lost capacity at nearly the same rate as each other (0.066%/cycle), and gained in cell impedance at nearly the same rate (0.076%/cycle). A total of about 33% of the capacity loss can be attributed to the side reaction.

- The room temperature cell cycled to only 70%DOD showed the slowest rates of capacity fade (0.014%/cycle) and impedance rise (0.01%/cycle), with a large fraction of the capacity fade (57%) due to the side reaction.

The rest of the paper is concerned with the various diagnostic techniques aimed at understanding the reasons for these differences in capacity fade and impedance rise.

XRD Analysis of the Cathode

XRD was carried out on the four cathodes discussed in this work. All of the cathode samples were at a mid-SOC, despite having been fully discharged at C/25 before disassembly. The SOC's of the various cathodes, determined by matching lattice parameters as discussed previously [7], compare reasonably well with the lithium removed from the discharged cathode sample in the half-cell test (see Table 2). Also shown in Table 2 are the crystallite sizes derived from the XRD peak widths. It appears that any type of cycling results in a reduction in the crystallite size, with a possible acceleration of this phenomenon for the cell cycled at 60°C. None of the XRD patterns for cathode samples removed from these cells showed any evidence of new phases that could be held responsible for some of the degradation, even for the cell cycled at 60°C. No X-ray analysis of the anodes was carried out.

MAS NMR Spectroscopy of the Cathode

^{7}Li MAS NMR spectra were acquired for the cathodes removed from the PG03, PG04, PG06, and PG13 cells as well as for a fresh cathode before cell assembly as shown in Figure 5 (spectrum for PG13 not shown). The NMR spectrum of the fresh cathode contains a broad resonance at approximately 505 ppm and a sharp resonance at 0 ppm. The observation of two resonances agrees with the previous studies on a series of $LiNi_{1-y}Co_yO_2$ ($0 \le y \le 1$) samples performed by Marichael et al [10]. The Li cations in these materials are coordinated to 6 transition metal (TM) atoms in the first coordination environment through Li–O–TM bonds with a 90°-bond angle and 6 transition metal atoms in the second coordination environment through Li–O–TM bonds with a 180°-bond angle [11]. The coupling between the unpaired electron of Ni^{3+} and the Li nucleus gives rise to a hyperfine shift, whereas diamagnetic Co^{3+} (e_g^6 t_{2g}^0) and Al^{3+} will not contribute to any hyperfine shift [10]. Thus, the resonance at 0 ppm is assigned to Li surrounded by 12 Co/Al atoms in the 1st and 2nd coordination spheres and the broad resonance centered at 505 ppm is assigned to Li containing more than one Ni^{3+} in the coordination sphere. The large linewidth of the resonance at 505 ppm indicates a dispersion in the local environments. The combination of different numbers of Ni^{3+} and Co^{3+} (or Al^{3+}) in the coordination sphere gives rise to different hyperfine shifts, resulting in the overlap of several resonances. The resonances at 0 and 505 ppm will be denoted as Li with Co/Al-neighbors and Li with Ni-neighbors, respectively. If Ni^{3+}, Co^{3+}, and Al^{3+} are homogeneously distributed in the cathode particles, a broad single resonance showing a Gaussian distribution is expected, which is contrary to our observation. Therefore, ^{7}Li NMR data show the existence of Co clusters in $LiNi_{0.8}Co_{0.15}Al_{0.05}O_2$.

Compared to the spectrum of the fresh electrode, the resonance for the Li with Ni-neighbors was observed at lower shifts of 492, 456, 387, and ~300 ppm for the cathodes from PG04, PG06, PG03, and PG13 cells, respectively.. All three electrodes show a sharp resonance at 0 ppm without a significant change in the peak position and the intensity. As the Ni^{3+} cations are oxidized to Ni^{4+}, the resonance for Li with Ni-neighbors will exhibit smaller shifts due to the decreased number of Ni^{3+} in the coordination environment of the Li. This indicates that the electrodes from the cycled cells were not fully discharged, and some of the Ni is in the +4 state. It was reported that the Li NMR signal loses intensity

due to the electronic hopping between Ni^{3+} and Ni^{4+} when the $LiNi_{0.3}Co_{0.7}O_2$ cathode is partially charged [11]. The signal, which is affected by the hopping process, cannot be refocused with an echo pulse sequence and the loss in the signal intensity due to the different mobility needs to be considered. Nonetheless, it is clear that the cycled electrodes show decreased signal intensity from Li with Ni-neighbors. Therefore, both the shift in the peak position and decreased intensity indicate that the cycled cells are not in a fully discharged state. Considering the peak position and the signal intensity, the SOC is in the order of PG13<PG03<PG06<PG04, with values of the relative state of charge (referred to PG04) listed in Table 3. These results are reasonably consistent with the electrochemical and XRD results also shown in Table 3.

FTIR Analysis of the Cathode

A typical infrared spectrum from the PG03 cathode is shown in Fig.6. The FTIR spectra from all four cells were essentially identical (the backgrounds were different due to differences in surface morphology). Although weak peaks characteristic of the carbonyl group in EC (at 1804 cm^{-1} and 1774cm^{-1}) were still discernable, features in the spectral regions between 1300 cm^{-1}– 700 cm^{-1} are the most prominent and are not solvent or electrolyte related. Most of these features could be readily assigned to PVDF, as shown by comparison with the reference spectrum from a PVDF powder (Fig. 6a). Interestingly, the spectral difference in the 1600 cm^{-1} to 1300 cm^{-1} region between that from the virgin cathode (before assembly into a cell) and that after cycling in the cell was quite striking. The strong peak at 1416 cm^{-1} and a shoulder at 1500 cm^{-1} are the C-O asymmetric and symmetric stretching modes of Li_2CO_3. There should also a sharp peak at 870 cm^{-1} associated with (CO_3^{-2}) group bending mode, to confirm the assignment definitively. Unfortunately, this peak is superimposed on a strong, sharp peak at 875 cm^{-1} from the PVDF. Interestingly, no residual lithium carbonate was detected in the spectra of any of the cathodes of cycled cells, as clearly indicated by the absence of the strong peak at 1422 cm^{-1} and its shoulder at 1493 cm^{-1}. The fate of the Li_2CO_3 during the cycling is still unknown. Furthermore, there is no evidence of any insoluble (in **DEC**) film on the cathode produced by reaction with the electrolyte. Products formed by decomposition of

the electrolyte salt, $LiPF_6$, can be difficult to detect with IR spectroscopy. The principal product observed by other techniques, such as XPS [12] is LiF, but LiF is invisible in the mid-IR (700 – 4000 cm^{-1}) region available in our spectrometer. The absence of LiF in our spectra is not indicative of its absence in the passive films on these cathodes.

MicroRaman Analysis of the Cathode

Selected Raman microprobe spectra taken from different locations at PG04, PG06, PG03 and PG13 cathodes are shown in Figure 7. A typical Raman spectrum of a fully discharged composite $LiNi_{0.8}Co_{0.15}Al_{0.05}O_2$ cathode is dominated by a broad band centered around ~ 500 $cm^{-1}$with a little shoulder at 558 cm^{-1} and two bands at ~1360 and ~1580 cm^{-1} which correspond to the $LiNi_{0.8}Co_{0.15}Al_{0.05}O_2$ and the D and G bands from the carbon additives (discussed below), respectively. On the other hand, the Raman spectrum of $LiNi_{0.8}Co_{0.15}Al_{0.05}O_2$ active material changes significantly upon application of excessive power of the laser beam. At intensities >0.5 mW the broad band at ~500 cm^{-1} converts into one sharp peak at 510 cm^{-1} (not shown here) similar to the spectra of $LiNi_yCo_{1-y}O_2$ reported in [13,14].

Interestingly, the cathodes from the room temperature cells i.e., PG04, PG06 and PG03 exhibited a mixture of fully discharged and partially charged particles of $Li_{1-x}Ni_{0.8}Co_{0.15}Al_{0.05}O_2$ at the surface, despite the cathodes being slowly discharged before sampling. However, the surface of the PG13 cathode consisted of fully charged active material. Moreover, microprobe Raman spectra from different locations at the surface of the tested cathodes displayed a sharp band at 1009 cm^{-1} accompanied by two side-bands at 642 and 1106 cm^{-1}, (spectrum C in Fig.7), which are characteristic for lithium pyrophosphate. There were also areas on the surface of the tested cathodes, which showed very broad and featureless maxima centered around ~550 and 1050 cm^{-1}. Their origin is most likely phosphate-type compounds that are products of $LiPF_6$ decomposition [14].

In addition to the individual spectra from different locations, cathode surface average spectra were produced with the Raman microscope. Raman spectra were collected from 52x75 μm sections of the surface of cathodes at 0.7 μm resolution and averaged into one representative spectrum for each cathode. Micro Raman surface average spectra of the

virgin cathode, PG03, PG04, PG06 and PG13 cathodes are shown in Figure 8. The intensity ratio between the three major bands at ~510 cm^{-1} ($LiNi_{0.8}Co_{0.15}Al_{0.05}O_2$), and 1350, 1580 cm^{-1} (carbon) represent a semi-quantitative comparison because of the different Raman cross-section of $LiNi_{0.8}Co_{0.15}Al_{0.05}O_2$ and carbon. However, it is clear from Fig. 8 that active material/carbon surface concentration ratio increases with the cathode degradation and is noticeably higher for the cell cycled 1000 times at 100% DOD compared with that cycled 1000 times to 70% DOD. The most drastic change in the in the active material/carbon surface concentration ratio was observed in the high temperature cell (PG13). Previous results for the cathode cycled at 60°C showed a complete lack of conductivity of the cathode surface [7] consistent with either loss of contact of particles at the electrode surface with the rest of the electrode, or presence of a non-conductive film. A reduction in the conductive nature of portions of the electrode can easily explain rises in the cell impedance as well as losses in capacity through isolation of active material. This represents the clearest difference in the nature of the cathodes after the different DOD cycling.

TEM of the Cathode

TEM observations were carried out with cathode samples from the room-temperature-cycled cathodes. In Fig. 9, a layer of about 5 nm thick is clearly evident on the surface of a $LiNi_{0.8}Co_{0.15}Al_{0.05}O_2$ grain from the PG03 cathode. The lattice fringes of 0.24 nm represent the (006) crystal plane of the $LiNi_{0.8}Co_{0.15}Al_{0.05}O_2$. An EDX spectrum (not shown) of the entire image area indicated the absence of significant impurities. It does show traces of P, which could be present from insoluble P-containing degradation products from the electrolyte salt, consistent with the results from the Raman spectroscopy. From the previous discussion of the FTIR results, this is not an organic layer, and it is not a carbonate layer, which is clearly removed with cycling by this time. In addition, it is not expected to contain metallic components due to the transparent nature of the film.

Many defects, stresses, and dislocations were directly observed in $LiNi_{0.8}Co_{0.15}Al_{0.05}O_2$ grains as shown in Fig. 10. This kind of edge dislocation (circled) involves the removal of one-half of a (104) lattice plane of atoms from the crystal. Some

small lattice disorder was found in the $LiNi_{0.8}Co_{0.15}Al_{0.05}O_2$ grains as shown in Fig. 10. The position marked with an arrow shows a lattice-disordered island about 4 nm in diameter surrounded by well-ordered (003) lattice fringes. The lattice expansion was also demonstrated by the TEM lattice images in Fig. 11. Some (003) lattice planes were expanded to 5 Å. Compared to the original fresh $LiNi_{0.8}Co_{0.15}Al_{0.05}O_2$ crystal, the (003) lattice plane was expanded by 6% due to cell cycling. This lattice expansion is in contrast to the contraction expected for a partially charged cathode, as measured with XRD. The large degree of defects in the TEM of some of the particles suggests that strain is building up in parts of the cathode. This is followed by a crystal dislocation and a relaxation of the lattice. These observations can lead to possible mechanisms for the impedance rise and possible isolation of material in the cathode. However, quantification of these observations was not possible and we could not quantify any differences between the cathodes cycled at room temperature, under different DOD.

MicroRaman Analysis of the Anode

Raman spectroscopy is a particularly useful tool for characterizing the near-surface structure of graphite because of its relatively large Raman scattering cross-section. A typical Raman spectrum of graphite consists of two E_{2g} active modes: a strong (G) band at ~1582 cm^{-1} and a weak band at 42 cm^{-1}, which is difficult to observe. However, decreasing intra-planar (L_a) and inter-planar (L_c) graphite microcrystalline dimensions always gives rise to a new feature at ~1360 cm^{-1}. This (D) band, which is assigned to the A_{1g} mode, is associated with the breakage of symmetry occurring at the edges of graphite sheets. The relative intensity of the D band *vs*. G band is attributed to increased carbon disorder [15,16].

Average Raman spectra of a fresh MAG-10 graphite anode and the anodes from PG04, PG06, PG03 cells cycled at room temperature, and the anode from PG13 cycled at 60°C are presented in Fig. 12. The spectrum from a freshly-formed anode is not statistically different from the anode never contacted by the electrolyte. The relative D and G peak intensity changes noticeably for the anodes from the cycled cells. The D/G band intensity ratio increases gradually in the room temperature cells with the increasing number of

charge discharge cycles. However, the most dramatic spectral change is observed for the anode cycled at 60°C, which is expressed by the huge increase of the D/G band intensity ratio and broadening of the G band. The increase of relative average D/G intensity ratios for the cycled anodes indicates that severe structural damage was induced into the graphite during cycling, especially at elevated temperature [16]. The ratio of the integrated peaks from each anode is shown in Table 4. The growth of the D-band is due to structural breakup of graphene planes in the MAG-10 graphite particles. The correlation between the various results summarized in Table 4 will be discussed below.

FTIR Analysis of the Anode

Fig.13 shows typical spectra obtained from the anodes of the four cycled cells. These spectra were qualitatively similar, but quantitatively different. Specifically, the relative ratio of features between 1700-1550 cm^{-1} and those between 1550-1140 cm^{-1} vary significantly among these cells. However, the overall spectral features from different cells could be fit with the same mixture of lithium compounds. The FTIR spectrum from the PG04 anode in Fig.13 was simulated (see Fig.14) by the superposition of individual spectra for lithium carbonate (Li_2CO_3), lithium formate (LiOOCH), lithium succinate ($LiO_2CCH_2CH_2CO_2Li$), and lithium methoxide ($LiOCH_3$). A small amount of methanol was also observed on some anodes, but is not shown here. The features in the 1674-1550 cm^{-1} spectral region come exclusively from lithium carboxylates, while those in the 1550-1140 cm^{-1} region come mainly from lithium carbonate. The two sharp features at 1600 cm^{-1} and 1576 cm^{-1} are the spectral signatures of the carboxylate (–COOLi) functional group, which we have chosen to model using lithium formate and lithium succinate, respectively. Other carboxylates such as acetate or propionate, may also be present. The variation in peak ratio in these two spectral regions reflects the relative abundances of carboxylate versus carbonate in the layer. It is evident from Fig.13 that the anode from PG13, the cell cycled at high temperature, has a uniquely different spectrum from the room temperature cycled cells, PG03, PG04 and PG06, having the most carbonate (Li_2CO_3) and least carboxylate content.

Carboxylates are not among the lithium compounds typically reported as components of the passive film on Li-ion battery anodes [17]. It is possible that the appearance of carboxylates in the passive films on these particular anodes is coupled to the content of the cathode material, i.e. the carbonate layer on the surface of the $LiNi_{0.8}Co_{0.15}Al_{0.05}O_2$. We know that the carbonate layer on the surface of the $LiNi_{0.8}Co_{0.15}Al_{0.05}O_2$ decomposes during the cycling, probably producing CO_2. It is known that CO_2 is electrochemically reduced in the presence of water [18] via following mechanism:

$$CO_2 + e^- \leftrightarrow \bullet CO_2^-$$

$$\bullet CO_2^- + H_2O + 2\,Li^+ \rightarrow HCOOLi + LiOH$$

It is also known that electrochemical reduction of DEC occurs via formation of ethyl radicals as an intermediate [19], and if CO_2 reduction is occurring simultaneously more aliphatic carboxylates are also formed, e.g. propionate and succinate

$$CH_3CH_2\bullet + \bullet CO_2^- + Li^+ \rightarrow CH_3CH_2COOLi$$

$$CH_3CH_2COOLi + \bullet CO_2^- + Li^+ \rightarrow \bullet CH_2CH_2COOLi + HCOOLi$$

$$\bullet CH_2CH_2COOLi + \bullet CO_2^- + Li^+ \rightarrow LiO_2CCH_2CH_2CO_2Li$$

It is in general not possible to estimate by ATR-FTIR the differences in thickness or amount of material in surface films, particularly on rough surfaces like these, and we have not done so. However, the integrated peak height ratios for the inorganic component to the organic components were calculated for each anode and are listed in Table 4. This type of calculation is not susceptible to differences in the surface morphology of the electrodes.

From an initial glance at Table 4, there appears to be a correlation between the ratio of organic to inorganic content of the passive film and the cycling conditions. It appears that there is either an increase in the inorganic component with cycling or a conversion from organic to inorganic. Without the absolute layer quantities, these phenomena cannot be distinguished. However, it is tempting to look for correlations between this inorganic to organic SEI component ratio, the increasing disorder in the anode graphite and various measures of capacity and power fade in the cells.

Discussion

Li-ion cells with the Gen 2 chemistry have been subject to a large amount of diagnostic evaluation within the ATD program, as well as in this study. In the ATD program, 45 18650 cells were subjected either to calendar-life studies at 60% SOC and temperatures up to 55°C [6,20] or to a controlled-power life-cycle test profile mode emulating the requirements of an HEV battery, the 25 Wh Power-Assist Life-Cycle (PALC) profile [20]. This pulse profile is 6 min. in length, involves high power discharge and regen pulses and is nominally charge neutral. These cycles span a very narrow SOC window around 60% SOC and they are repeated many thousands of times. For the cells reported here, the life-testing is different in two major respects. Firstly, the cells are cycled over an order of magnitude larger span in SOC, and the time of the testing is significantly shorter. Some of the ATD cells have been under test as long as 68 weeks. It is interesting to compare the performance decline between the BATT and ATD cells at the same level of capacity throughput. For this comparison, one needs an estimate of the number PALC profiles to pass an amount of charge equivalent to the rated capacity of the cell. We calculated an equivalent of about 77 PALC cycles per 100% DOD cycle, or 435 full 100% DOD cycles per 4-week test period in the ATD program. We can compare the performance of the PG04 and PG06 cells with a 4-week room temperature cell from the ATD program. The ATD cells showed an equivalent of 4% power fade and 6% capacity fade (at C/25) at this time in their life [21]. This provides a third point in the comparison of performance fade as a function of DOD during cycling, or alternatively the span of SOC during cycling. This suggests that higher DOD cycling is more stressful to the cells. The reasons for this will depend on which electrode is causing the performance decline.

The ATD program has observed two regimes of performance fade with different time-dependencies. The first period of power fade, lasting on the order of 30-40 weeks, has been attributed to changes in the cathode. After this period, the behavior of the anode starts to limit the performance. The exact degradation processes in each of the electrodes is still a matter of some debate, however, the power fade in the cathode is being modeled as a logarithmic process that starts to level out as the linear decline in the anode performance takes over [21].

In this work, we have many fewer cells to examine and cannot form such an extensive picture of the time dependence of the performance decline. However, within the 11 weeks of these pouch cell tests, the anodes in all of these cells showed very little change in electrochemical performance when matched against a large source of cycleable Li. In fact, the consumption of the cycleable Li in the anode, which is probably only a factor in the degradation of the longest-lived cells (PG03 and PG06), is a linear process in time, as was shown in Fig. 4. The connection between the impedance growth in the anode and these diagnostic considerations is not shown but it is not unreasonable to consider that the thickness of the SEI might be expected to grow in a linear fashion with the consumption of the Li and if the side-reaction products are inorganic, the conversion of the nature of the SEI to mostly inorganic might also be expected to be linear.

The changes in the surface chemistry coincident with the consumption of Li were analyzed with FTIR and Raman spectroscopy, as presented above. The two anode diagnostic parameters presented above, namely the composition of the SEI layer on the anode and the extent of disordering of the original MAG-10 carbon, are re-plotted as a function of this Li loss for the room temperature pouch cells in Figure 15. Through 11 weeks, the correlation looks pretty good. It is probable that further conversion in the surface chemistry will take place at longer times and higher temperatures. The high temperature cell only showed a relatively small amount of Li consumption in the short test time, with a completely inordinate amount of the inorganic SEI, and this point is not shown. The rapid buildup of the D/G ratio and I/O ratios, reflects that another degradation mechanism operative at this temperature. The accumulation of inorganic products at the graphite particles will form a barrier to Li-ion diffusion and may also form a barrier for electrons to travel across the electrode and thereby reduce cell power capabilities and electrochemical capacity. The absence of organic species in the passive layer would appear to be correlated to the capacity and power fade, i.e. an organic component is needed to have sufficient Li ion conductivity.

Peled et al. [22] found that the SEI on the graphitic plane cross-section is dominated by inorganic products whereas the basal planes are covered by a thin layer of organic polymers. Kostecki and McLarnon [16] found that the SEI layer on graphite electrodes changes in both morphology and chemical composition due to gradual structural

degradation of the graphite upon electrochemical cycling. This effect was particularly strong at elevated temperatures. Structural degradation of the graphite will lead to an increased anode surface reactivity with the electrolyte. A thick layer of inorganic products from side reactions is expected on the disordered carbon areas of the anode. The increased graphite disorder, i.e., an increasing concentration of freshly exposed active graphite edges, lattice defects, etc., induced upon cycling are effective electrocatalysts and react readily with the electrolyte to form inorganic products such as phosphates, carbonates, and LiF.

The early time degradation process is clearly more controlled by the behavior of the cathode, as demonstrated in the ATD program. It is clear from the electrochemical diagnostics that there is more happening to the cathode besides the loss of cycleable lithium. There is an impedance growth that is preventing the cathode from fully charging, even when supplied with a large amount of lithium in the half-cell. The primary conclusion from the cathode active material structure with XRD and Raman are that the cathodes removed from the different cells were at different states of charge, but there are no different phases present, at least not in the quantities predicted from the electrochemistry, as was observed for $Li_{1-x}Ni_{1-y}Co_yO_2$ [23,24]. Current-sensing atomic force microscopy imaging of $Li_{1-x}Ni_{1-y}Co_yO_2$ electrodes revealed that the cathode surface electronic conductance diminished significantly in the tested cells, and that the rate of change of the electronic conductance increased with cell test temperature [24]. More defects, dislocations and possible regions of isolation of parts of the cathode particles are observed for cathodes from the more highly degraded cells; however, quantification of differences between the different cathodes is not possible. The NMR showed that in comparison to the fresh cathode, the cycled cathodes exhibited a shift to lower frequency and decreased intensity of the Li NMR signals from Li with *Ni-neighbors,* whereas no noticeable change is observed for Li with *Co/Al-neighbors*. The change in Li signal with Ni-neighbors is the most severe for PG13, which shows the most capacity loss. This suggests that the capacity fade is caused by the change in the Ni-neighbors. In contrast, the Co-neighbor peak remains stable over prolonged cycling. It appears that the repeated cycling creates defects in the Ni-sites and increases the average oxidation state of the Ni, possibly from the formation of NiO_x as observed by TEM, other analyses of these types of cathodes [4].

Raman microprobe spectra do provide evidence of a surface species on the cathode that consists of phosphorous compounds such as lithium pyrophosphates, which originated from the decomposition of the $LiPF_6$ salt. The formation of such a layer was particularly visible in the PG13 cathode that was tested at elevated temperature. The amount and distribution of these phosphorous species was not uniform across the cathode surface but varied strongly with locations at which spectra were taken. The presence of inorganic product of the electrolyte decomposition contribute to the impedance buildup in the cathode and could lead to uneven current distribution, creation "hot-spots" and accelerated degradation of the cathode active material. Areas of P-containing film was also observed with TEM.

However, for all of these techniques, the cathodes were analyzed after washing in DEC. It is quite possible that there was some sort of soluble organic layer on the cathode that was removed during washing that is responsible for additional surface impedance. Detection and identification of such a layer will always be very difficult due to interference form the precipitated electrolyte components. For the high-temperature cell, we reported earlier that the cathode surface electronic conductivity was significantly reduced. It is possible that loss of electronic conductivity is related with the observed change of the active material/carbon surface concentration ratio change.

Conclusions

Cycling regime was found to have a large impact on the capacity and power fade mechanisms occurring in $LiNi_{0.8}Co_{0.15}Al_{0.05}O_2$/graphite pouch cells. From a comparison of cells cycled over 100% DOD and 70% DOD cycling with the ATD results for the very narrow (< 5% DOD) life-cycle pulse cycling, the performance decline was found to increase with the span of the SOC during cycling. Application of this cell chemistry in an EV battery should include a limit in the discharge to 70 or 80%DOD.

The loss of cycleable Li, most likely due to solvent reduction on the anode, was found to be linear in cell test time. In addition, the room temperature cells showed an SEI composition (inorganic vs organic fraction) and degree of graphite disorder on the anode surface, that roughly correlated with each other and with the extent of the Li consumption.

However, it is believed, from the post-test electrochemical analysis of the anode that this degradation was not the cause of the performance fade in the cells. Instead, in agreement with ATD cell results, it appears that the cathode degradation is the most important during the time these cells were tested. TEM and NMR showed evidence of crystalline defects and degradation of the Li-Ni environment, respectively, though no major new phases were identified, in agreement with the XRD results. Neither FTIR or Raman analysis of the cathode revealed no evidence of polymeric deposits on the cathode particles although both Raman and TEM did show evidence of P-containing deposits from electrolyte salt degradation.

A noticeable difference in the active material to carbon surface concentration ratio for the cycled cathodes that was observed by Raman mapping. The origin if this effect is still unknown and more work is clearly needed to understand exactly its mechanism and possible implications on the cathode electrochemical properties.

Acknowledgements

This research was funded by the Assistant Secretary for Energy Efficiency and Renewable Energy, Office of Advanced Automotive Technologies, U. S. Department of Energy, under contract number DE- AC03-76SF00098.

References

1. G. Nagasubramanian, R.G. Jungst, D.H. Doughty, *J. Power Sources*, **83**, (1999) 193
2. Q. Wu, W. Lu, J. Prakash, *J. Power Sources*, **88** (2000) 237.
3. R. Sutula"FY 2001 Progress Report for the Advanced Technology Development Program," U.S. DOE OAAT, February 2001.
4. X. Zhang, P.N. Ross, R. Kostecki, F. Kong, S. Sloop, J.B. Kerr, K.A. Striebel, E.J. Cairns, F. McLarnon, *J. Electrochem. Soc*., **148,** A463 (2001).
5. "Advanced Technology Development Program for Lithium-Ion Batteries: Handbook of Diagnostic Techniques," G.Henriksen, J. McBreen and F. McLarnon, eds., Lawrence Berkeley National Laboratory Report No. LBID-2464, Berkeley, CA., April 2003.
6. T.Q. Duong, *J. Power Sources,* **89**, 244 (2000).
7. J. Shim, R. Kostecki, T. Richardson, X. Song, K.A. Striebel, *J. Power Sources*, **112** 222, (2002).
8. J. Shim and K. Striebel, *J. Power Sources*, in-press, 2003.
9. S. V. Compton and D. A. C. Compton, in *Practical Sampling Techniques for Infrared Analysis*, P. B. Coleman (Ed.), CRC Press, Boca Raton, 1993, pp. 55-92.
10. C. Marichal, J. Hirschinger, P. Granger, M. Ménétrier, A. Rougier, C. Delmas, *Inorg. Chem*., **34**, 1773 (1995).
11. D. Carlier, M. Ménétrier, C. Delmas, *J. Mater. Chem*., **11**, 594 (2001).
12. D. Aurbach, B. Markovsky, A. Schechter, Y. Ein-Eli, H. Cohen, *J. Electrochem. Soc.*, **143**, 3809 (1996)
13. D. Ostrovskii, F. Ronci, B. Scrosti, P. Jacobsson, *J. Power Sources*, **94**, 183,(2001).
14. Zaban, D. Aurbach, *J. Power Sources*, **54,** 289, (1995).
15. R. Vidano, D.B. Fischbach, *J. Amer. Ceramic Soc.,* **61,** 13, (1978).
16. R. Kostecki and F. McLarnon, *J. Power Sources*, **119-121**, 550, 2003
17. D. Aurbach, *J. Power Sources,* **89** (2000) 206.
18. M. Hammouche, D. Lexa, M. Momenteau and J. Saveant, *J. Am. Chem. Soc*., **113**, 8455 (1991).

19. E.S. Takeuchi, H. Gan, M. Palazzo, R.A. Lessing and S.M. Davis, *J. Electrochem. Soc*., **144,** 1944 (1997).
20. *PNGV Test Plan for Advanced Technology Development Gen 2 Lithium-Ion Cells*, EVH-TP-121, Rev. 6, October 2001
21. J.P Christopherson, C.G. Motloch, I. D. Bloom, V.S. Battaglia, E.P. Roth and T.Q. Duong , "Advanced Technology Development For Lithium-Ion Batteries: Gen 2 Performance Evaluation Interim Report," INEEL/EXT-03-00095, February 2003.
22. E. Peled, D. Bar Tow, A. Merson, A. Gladkich, L. Burstein, D. Golodnitsky, *J.Power Sources*, **97/98,** 52, (2001).
23. R.V. Chebiam, F. Prado, A. Manthiram, *J. Electrochem. Soc*., **148**, A49, (2001).
24. R. Kostecki, F. McLarnon, *Electrochem. Solid State Lett.*, **5**, A164, (2002).

Table 1. Cell Performance

Cell	DOD (%)	Temp. (°C)	Cycles	Cell Power Fade	Cell ASI Increase @ EOD	Capacity Fade			
						Cell C/2	Cell C/25	Pos. C/25	Neg. C/25
PG13	100	60	140	NA	32%	65%	39%	59%	10%
PG04	100	25	480	70%	35%	30%	14%	18%	0%
PG03	100	25	1000	NA	78%	70%	40%	27%	0%
PG06	70	25	1000	45%	10%	14%*	11%	5%	0%

*from the 100%DOD C/2 cycle in the final RPT, the cell delivered of 70% capacity throughout 1000 cycles

Table 2 State of charge and other data from XRD and half-cell measurements on $LiNi_{0.8}Co_{0.15}Al_{0.05}O_2$ cathodes.

Cathode	SOC of Cathode	SOC from XRD	Crystallite size
fresh Gen 2	0	NA	66
PG04	23%	12%	52
PG03	39%	32%	56
PG06	13%	17%	51
PG13	63%	58%	41

Table 3. Comparison of Capacity Ratios

Cell Number	Electrochemical Capacity Ratio*	XRD Capacity Ratio*	NMR Capacity Ratio*
PG04	1.0	1.0	1.0
PG06	1.03	0.94	0.94
Pg03	0.70	0.77	0.74
Pg13	0.47	0.48	0.36

*PG04 taken as the basis for comparison

Table 4. Anode Diagnostics Summary

Cell	Peak intensity ratio: Inorganic to organic SEI components	D/G Integrated Band Ratio	Consumption of Li by side-reaction (%)	Duration of Cycling (months)
fresh anode	0	0.246	0	0
PG04	1.74	0.308	5	5
PG03	2.00	0.475	12	10.5
PG06	2.27	0.394	8	7.5
PG13	7.16	1.67	4	2

Figure Captions

Fig. 1. Discharge capacity of 12 cm2 pouch cells with of $LiNi_{0.8}Co_{0.15}Al_{0.05}O_2$/Mag-10 cells under different cycling regimes, 100%DOD: ◊ PG03, □ PG04, 70%DOD: × PG06, and 100%DOD at 60°C: o PG13.

Fig. 2. dQ/dV representation of C/25 test on the a fresh anode (——) and an anode harvested from a cell cycled at 100% DOD at 60°C (- - - -).

Fig. 3. Electrochemical diagnostics(post-test analysis) of a cathode sample, removed from the cell which had cycled 1000 times at 100%DOD and 25°C and cycled against fresh Li metal, (a) fresh cathode,(b) first post-test cycle, and (c) second post-test cycle.

Fig. 4. The extent of capacity loss by Li consumption in a side-reaction, calculated as shown in Fig. 3.

Fig. 5. ^{7}Li MAS NMR spectra of the fresh cathode and the electrodes extracted from the cells after cycling. The isotropic resonances are marked on the spectra. Spectra are plotted in an absolute intensity scale, taking into account the sample mass and the number of acquisitions.

Fig. 6. FTIR-ATR spectra for two cathodes and pure PVdF.

Fig. 7. Selected Raman microprobe spectra taken from different locations at (A) PG04, (B) PG06, (C) PG03 and (D) PG13 cathodes.

Fig. 8. Micro-Raman surface average spectra of the virgin cathode and cathodes from the tested cells.

Fig. 9. Lattice image & EDX spectrum of a $LiNi_{0.8}Co_{0.15}Al_{0.05}O_2$ grain with the SEI layer labeled by an arrow.

Fig. 10. Lattice image of the dislocation in a $LiNi_{0.8}Co_{0.15}Al_{0.05}O_2$ grain after cell cycling and power fade.

Fig. 11. Lattice image of small disordered area (marked by and arrow) & lattice expansion in a $LiNi_{0.8}Co_{0.15}Al_{0.05}O_2$ grain.

Fig. 12. Raman spectra of the anodes from the tested cells. From the lowermost to the uppermost curve are fresh anode, PG04, PG06, PG03, PG13, respectively.

Fig. 13. FTIR-ATR spectra from anode samples from four different cells.

Fig. 14. Comparison between the experimental ATR-FTIR spectrum from the PG04 anode and one synthesized from the following combination of components: 0.1 Li formate, 0.45 Li_2CO_3, 0.12 Li methoxide, 0.006 methanol and 0.015 Li succinate.

Fig. 15. Correlation between diagnostic results on the anode for the room temperature cells, □ FTIR data, o Raman data.

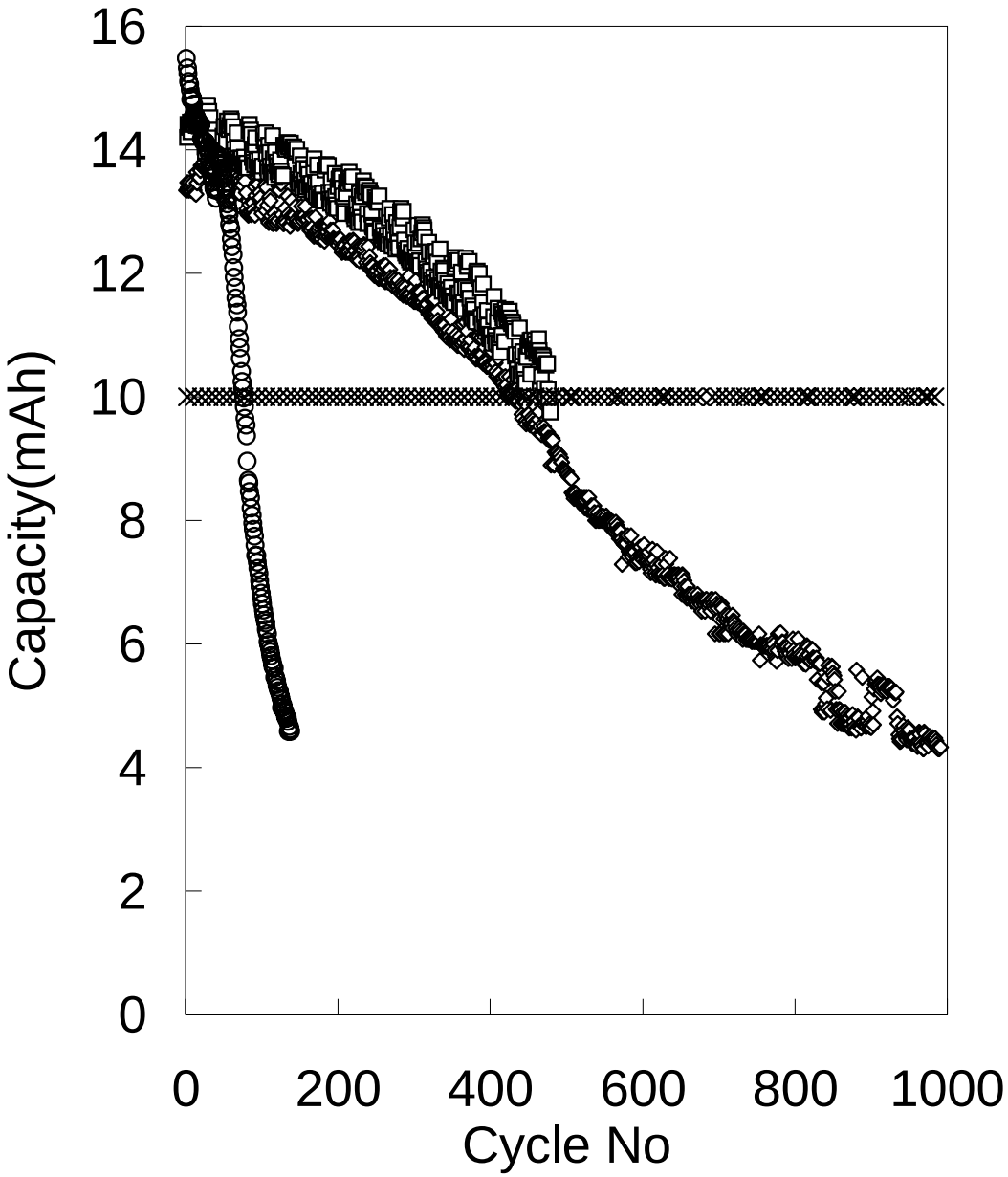

Figure 1

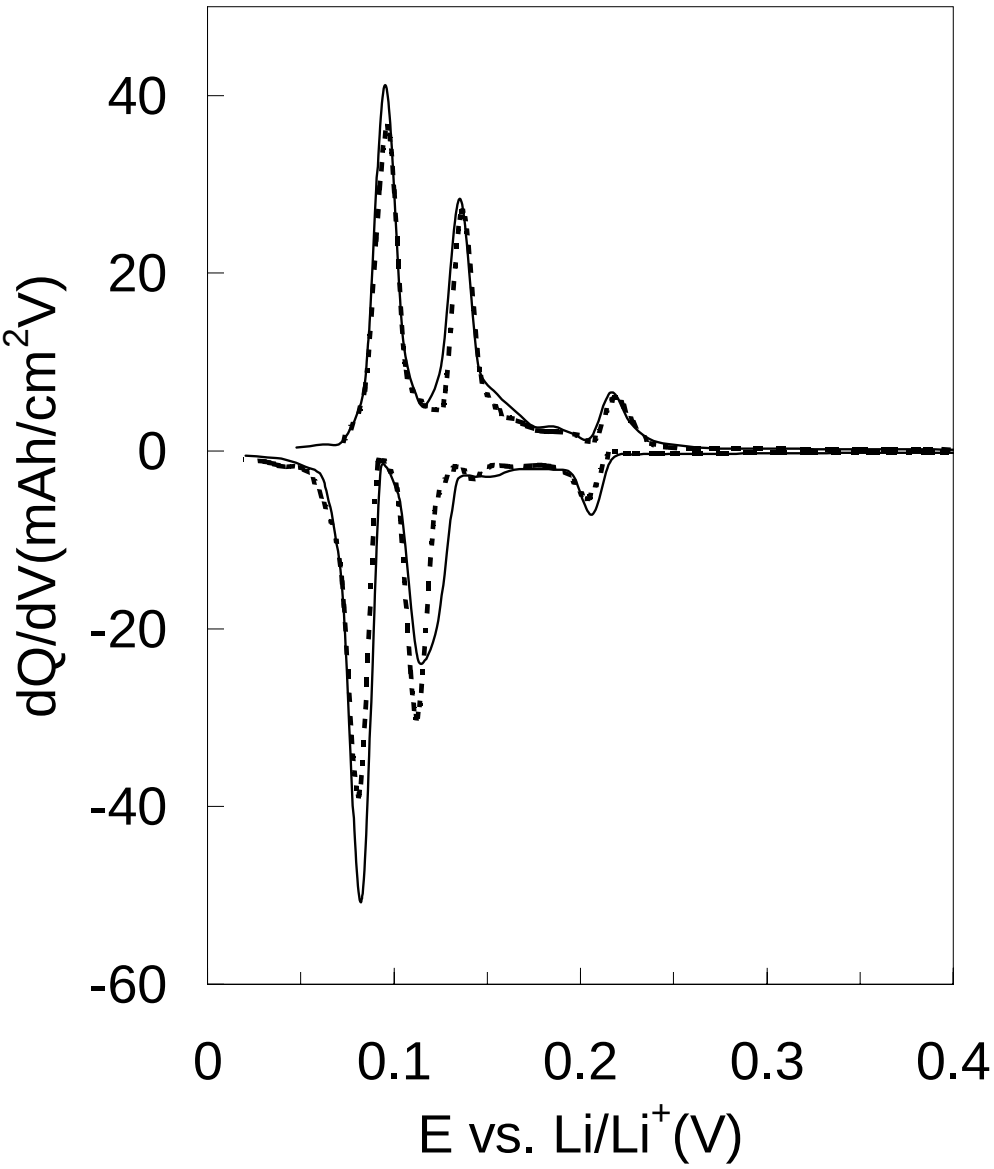

Figure 2.

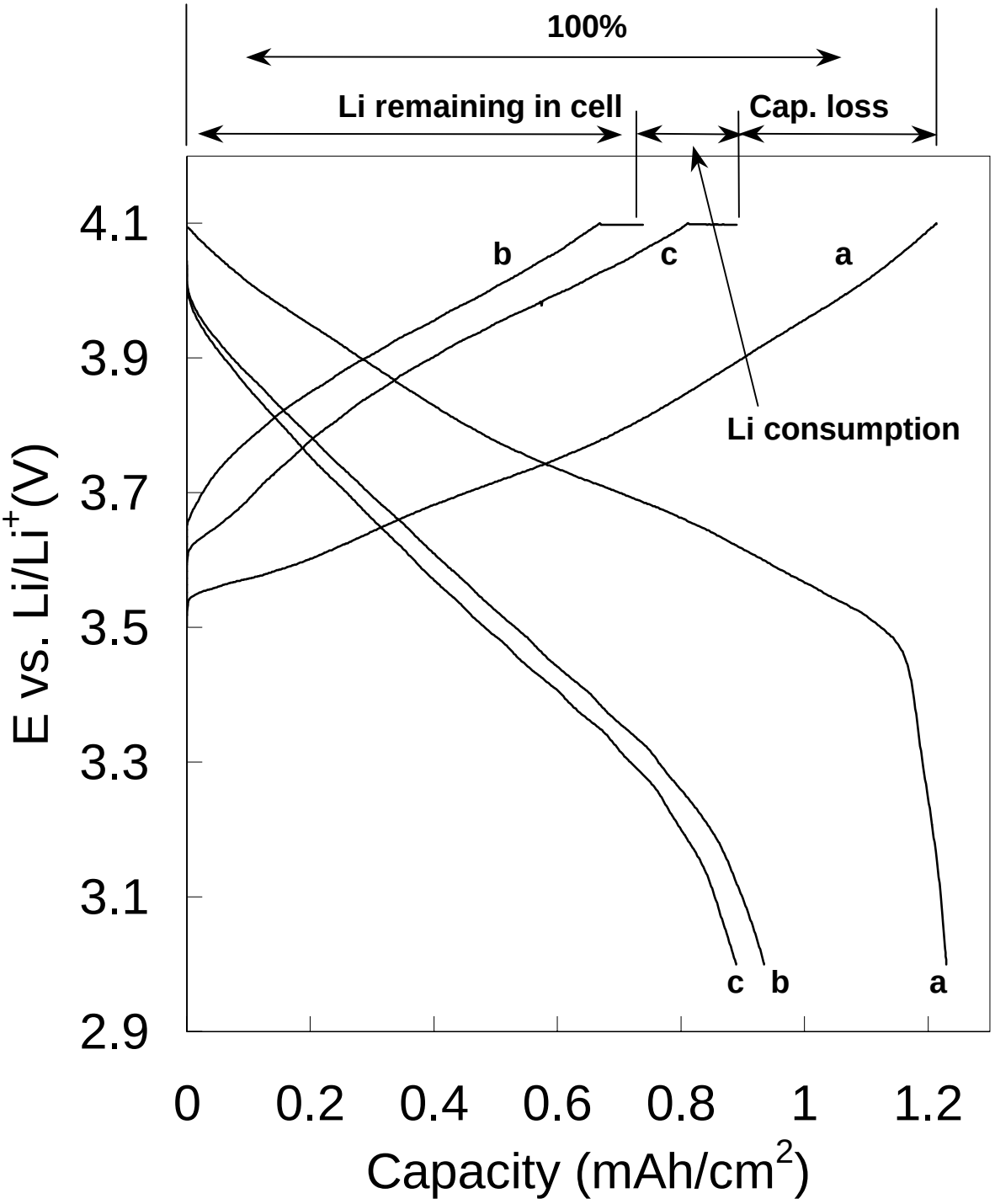
100%
Li remaining in cell
Cap. loss
4.1
3.9
3.7
3.5
3.3
3.1
2.9
E vs. Li/Li+(V)
b
c
a
Li consumption
c
b
a
0
0.2
0.4
0.6
0.8
1
1.2
Capacity (mAh/cm2)

Figure 3

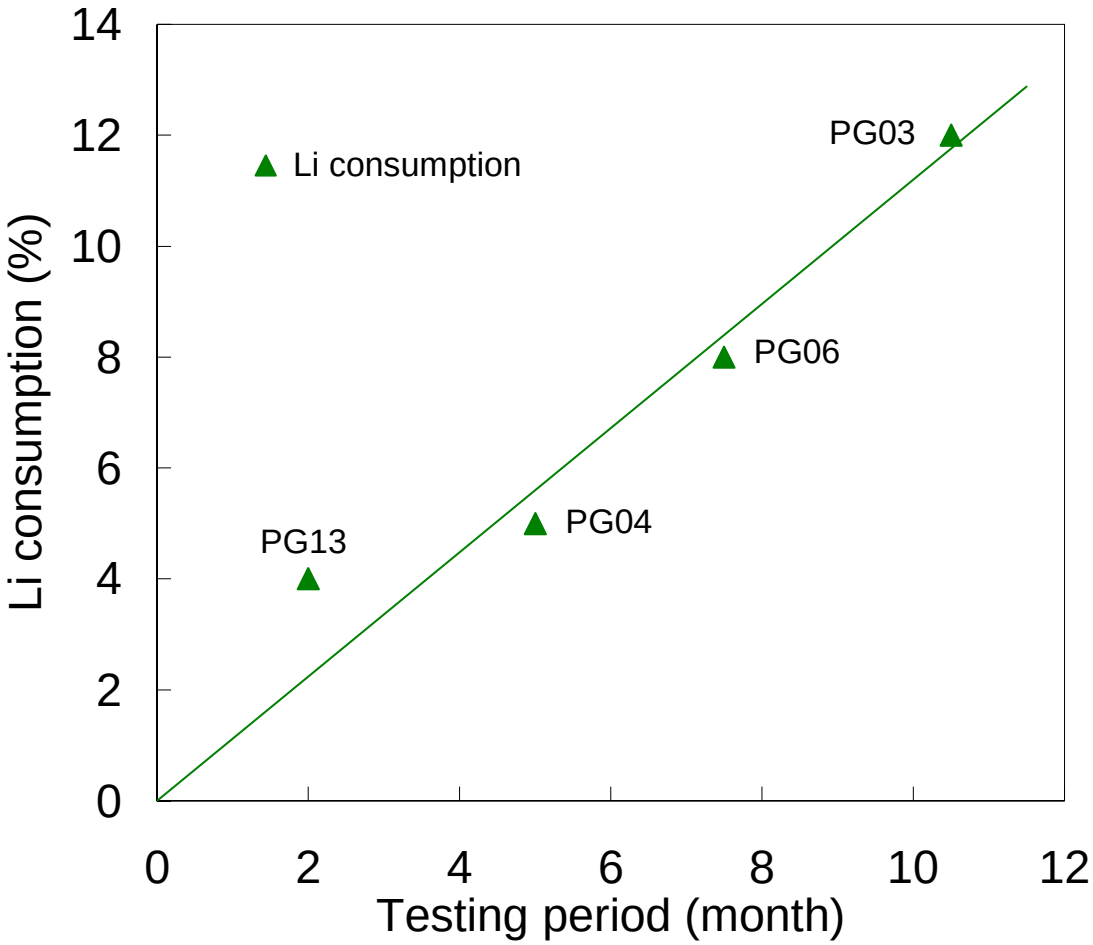
14
12
10
8
6
4
2
0
Li consumption (%)
Li consumption
PG03
PG06
PG04
PG13
0
2
4
6
8
10
12
Testing period (month)

Figure 4

Figure 5

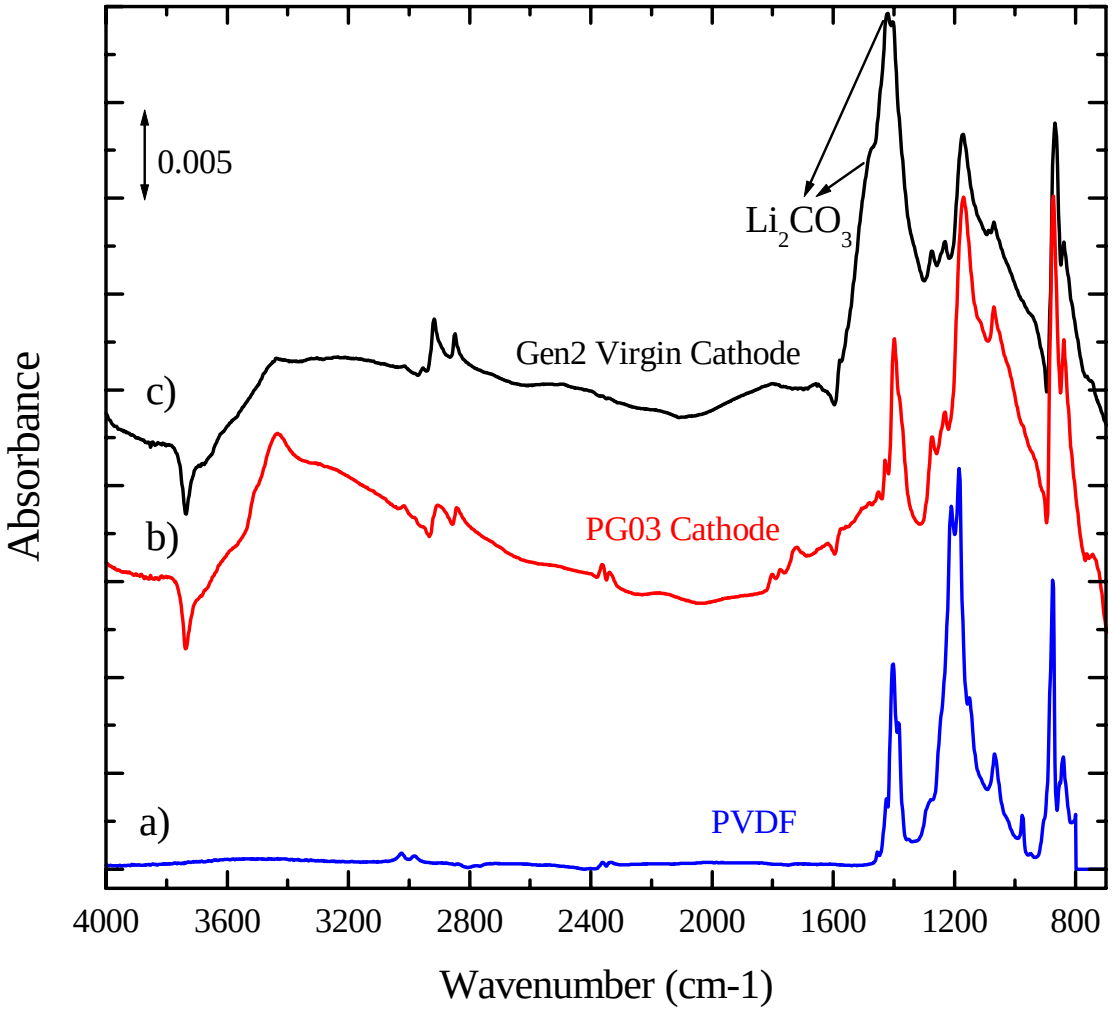
0.005
Li2CO3
Gen2 Virgin Cathode
c)
b)
PG03 Cathode
a)
PVDF
Absorbance
4000
3600
3200
2800
2400
2000
1600
1200
800
Wavenumber (cm-1)

Figure 6

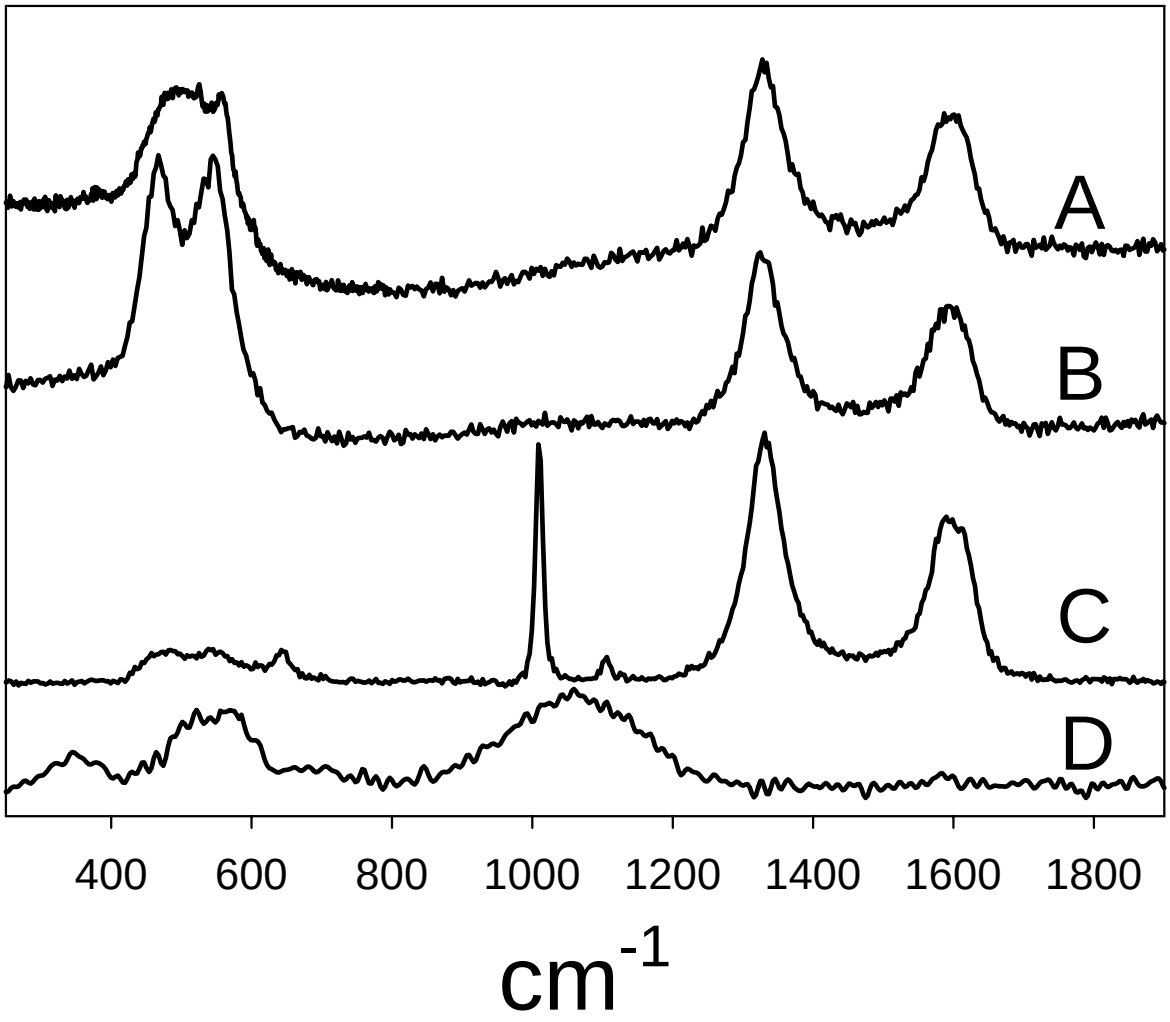

Figure 7.

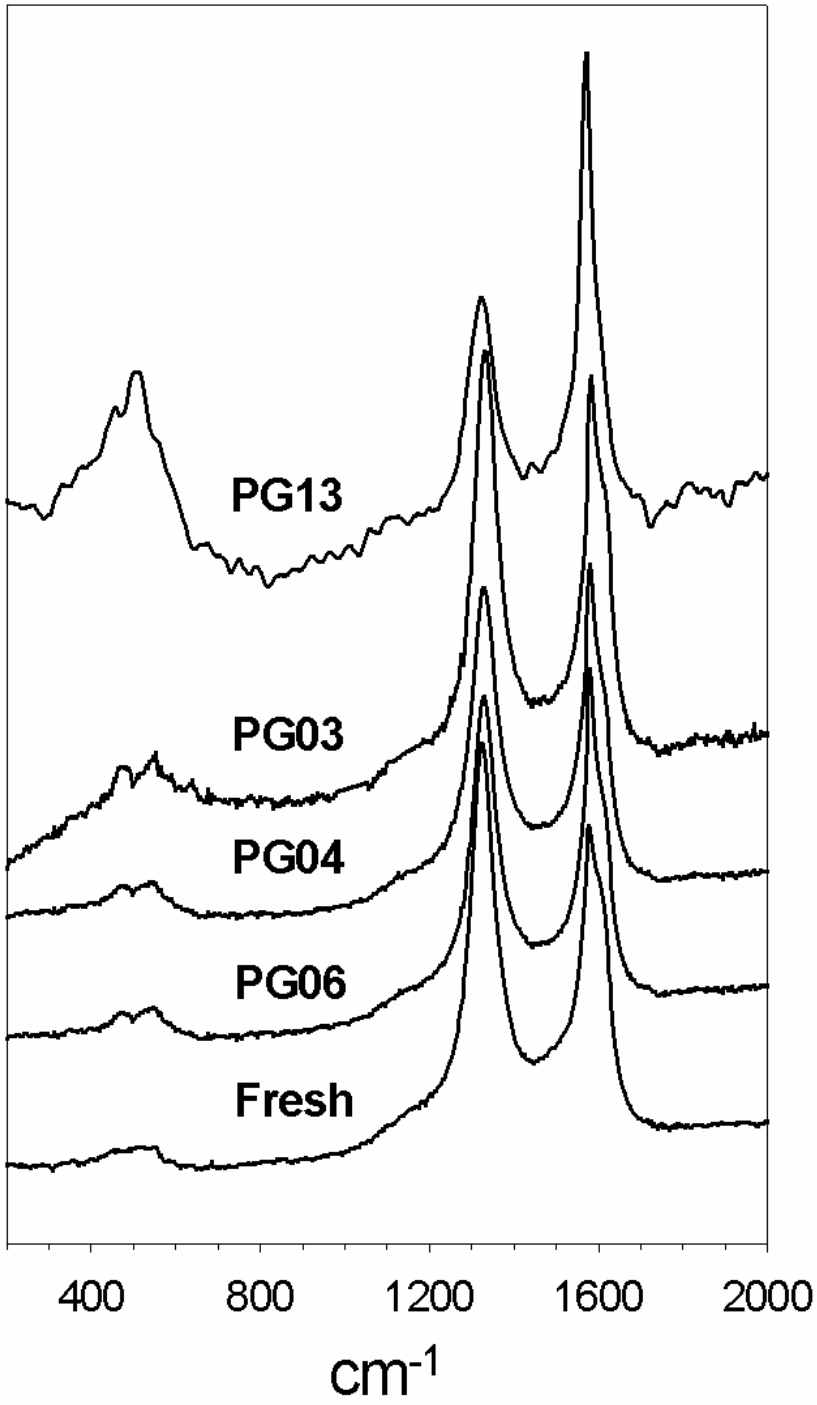

Figure 8

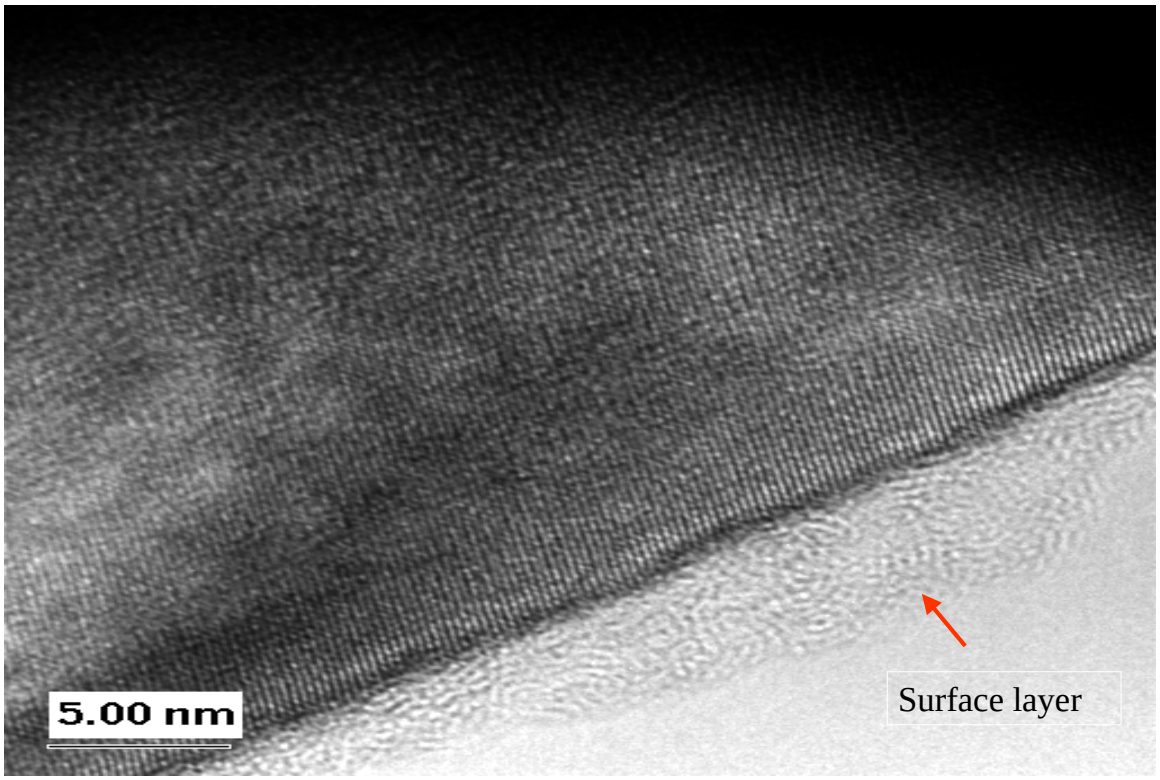

Figure 9

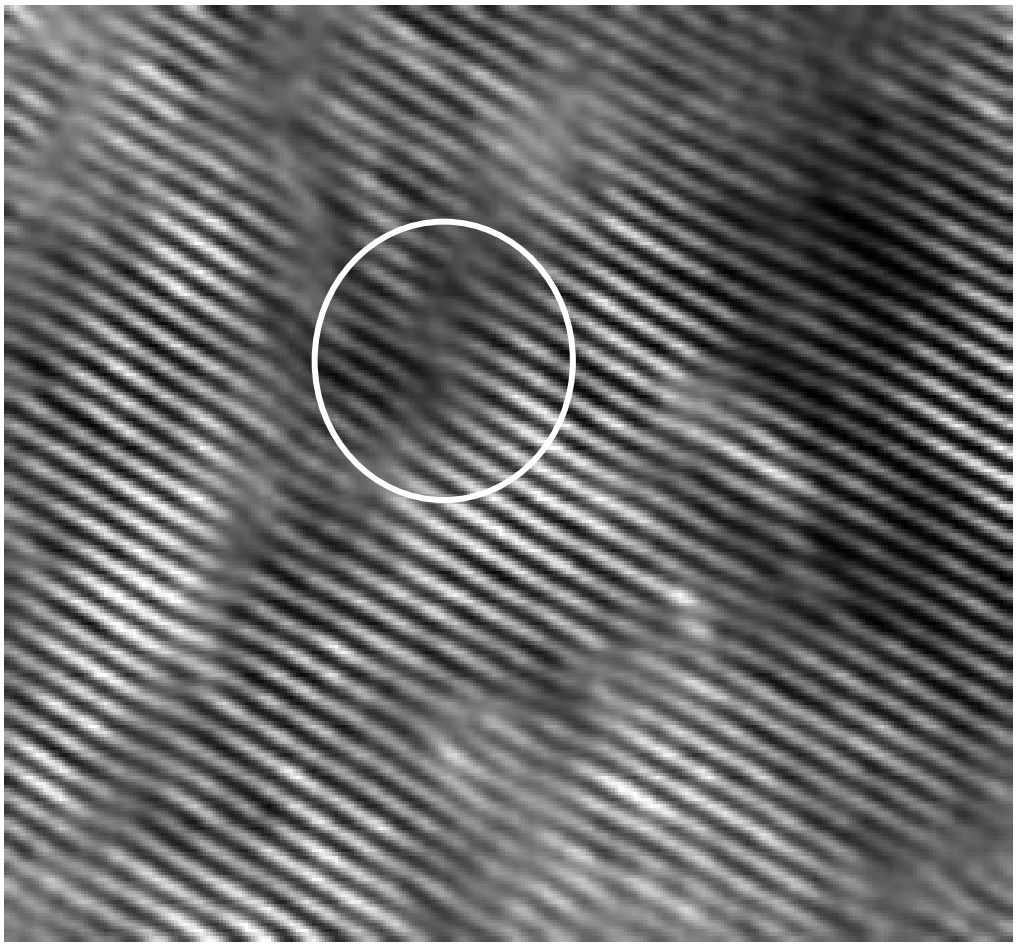

Figure 10

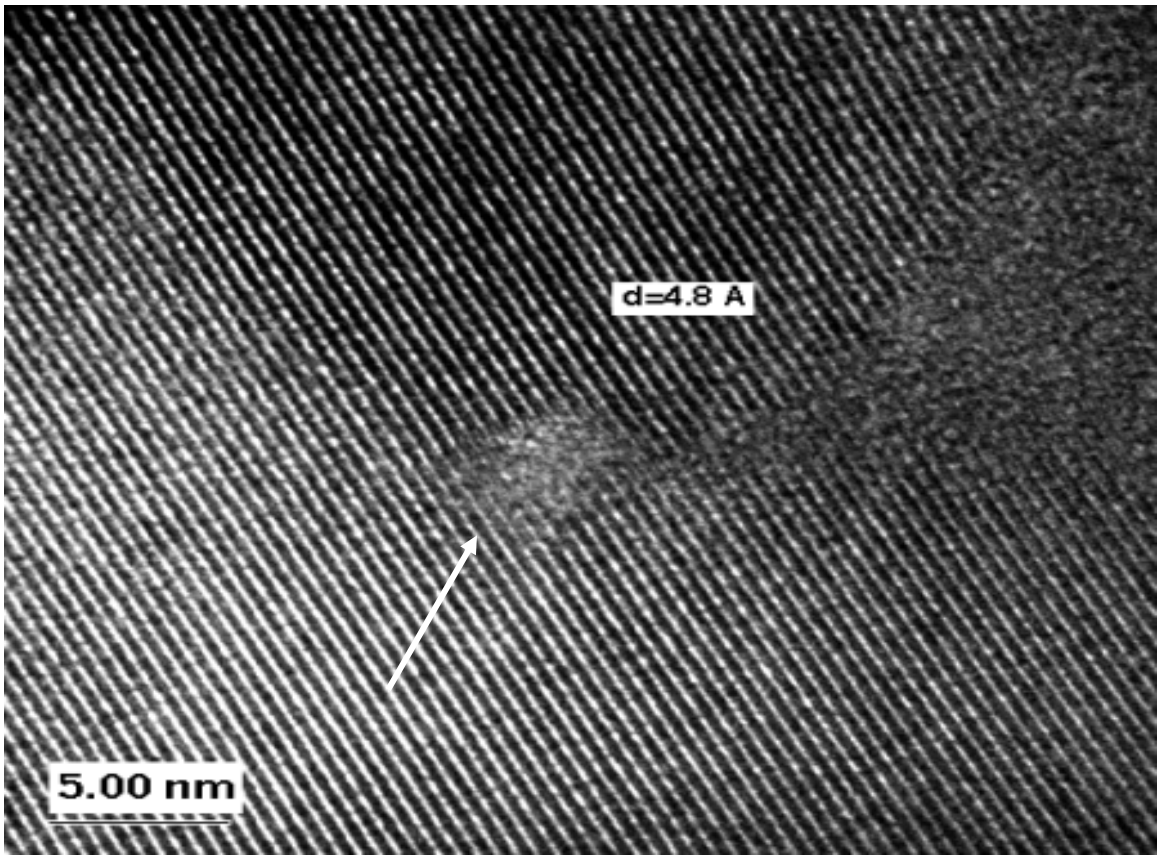

Figure 11

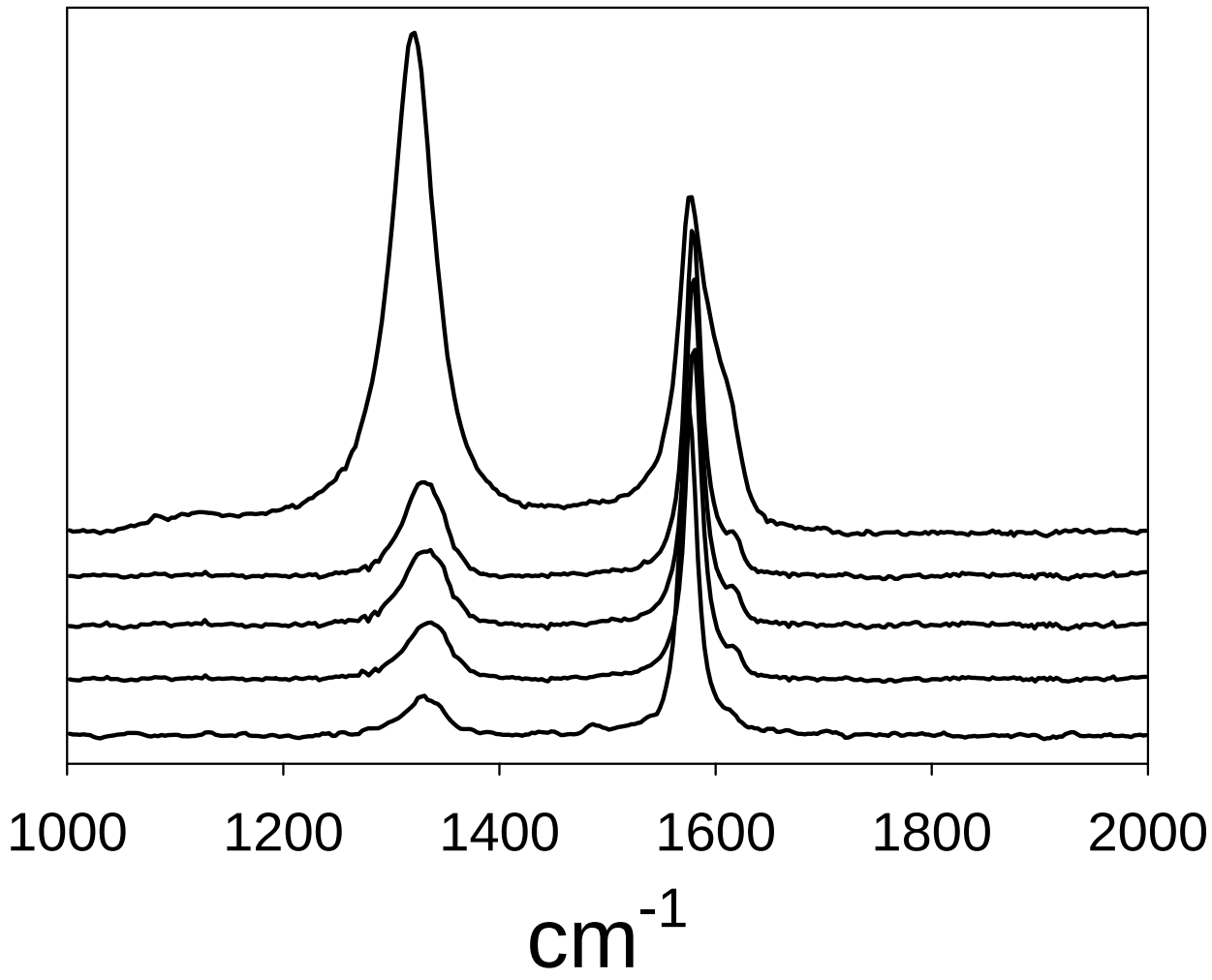

.

Figure 12

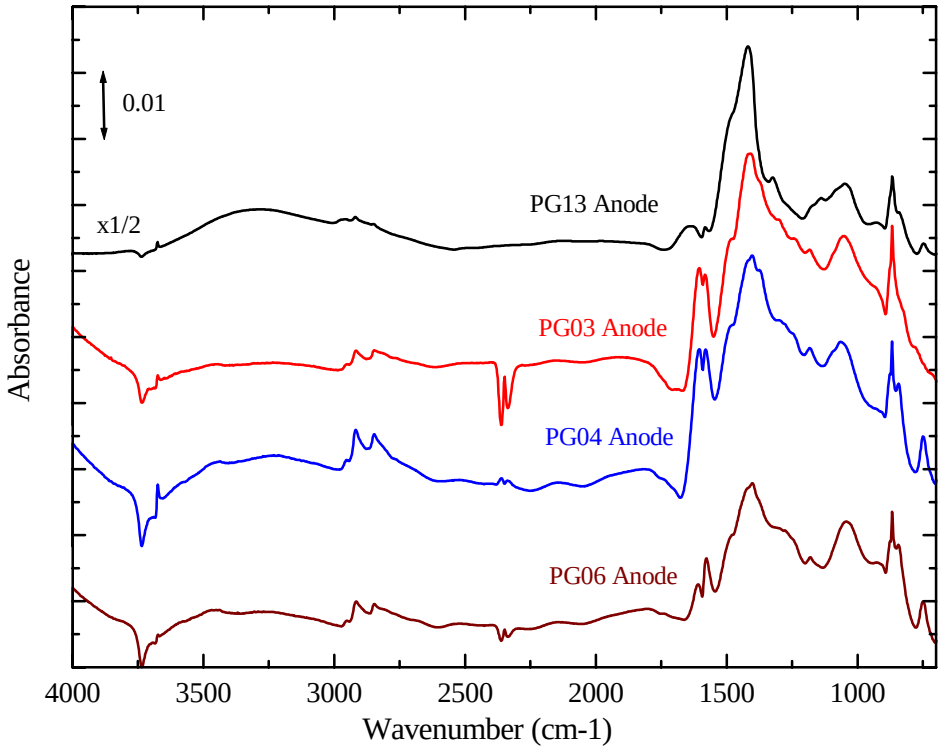
0.01
x1/2
PG13 Anode
PG03 Anode
PG04 Anode
PG06 Anode
Absorbance
4000
3500
3000
2500
2000
1500
1000
Wavenumber (cm-1)

Figure 13

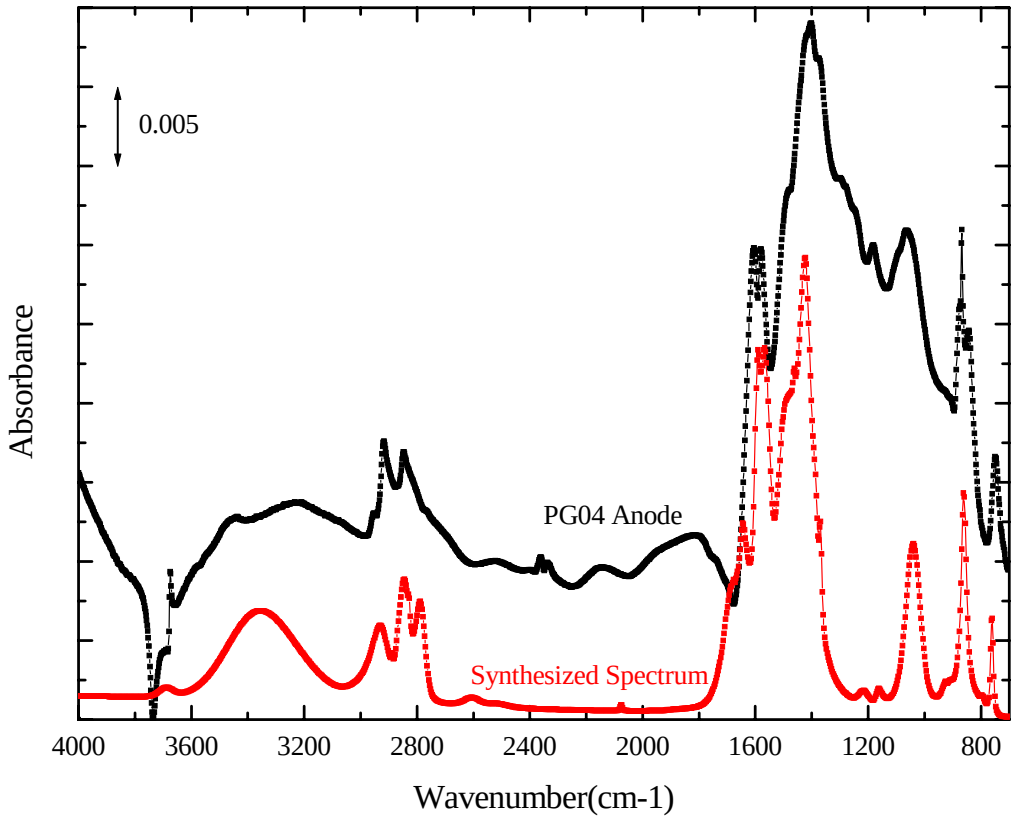
0.005
Absorbance
PG04 Anode
Synthesized Spectrum
4000
3600
3200
2800
2400
2000
1600
1200
800
Wavenumber(cm-1)

Figure 14

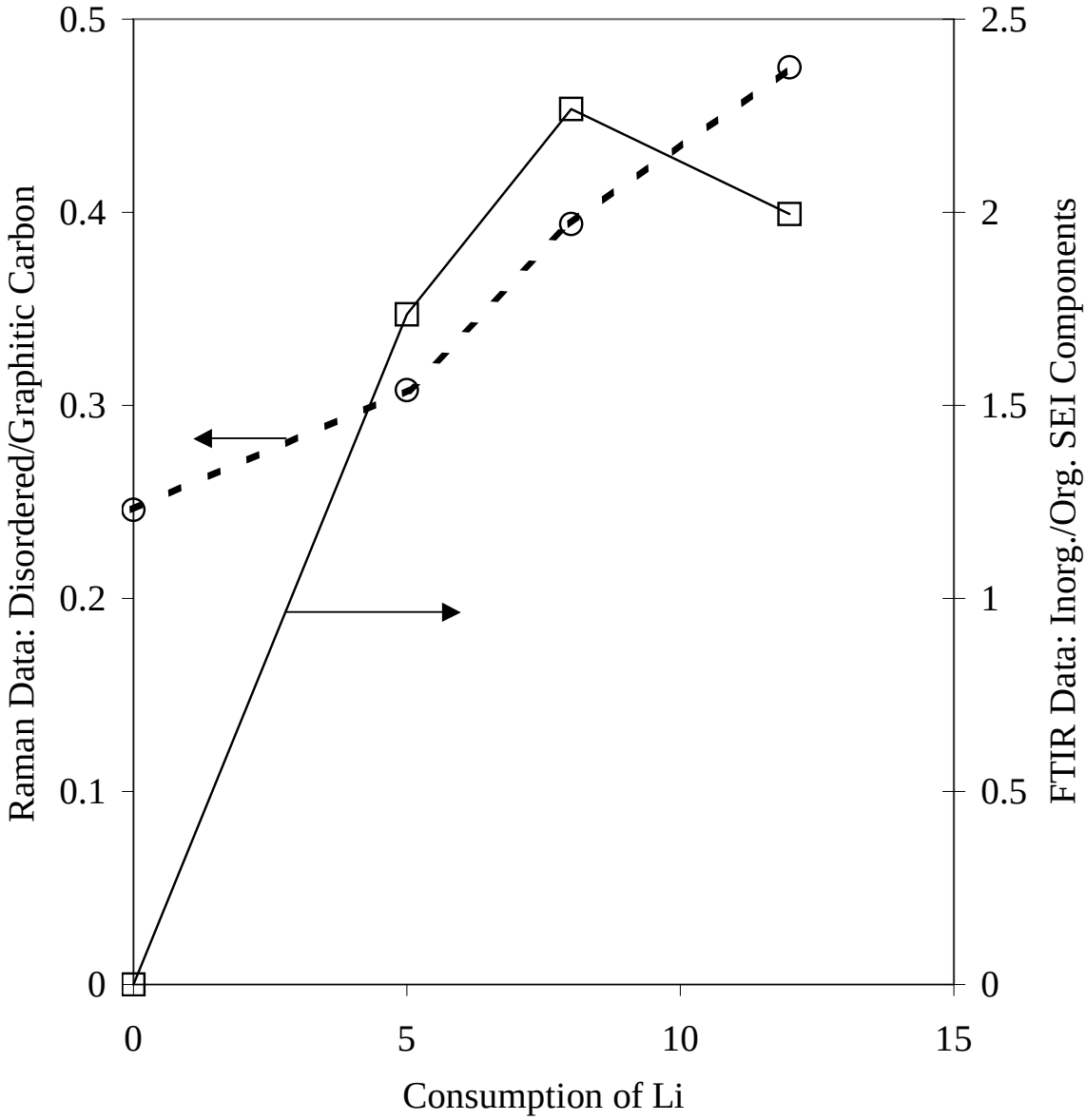
0.5
0.4
0.3
0.2
0.1
0
2.5
2
1.5
1
0.5
0
0
5
10
15
Raman Data: Disordered/Graphitic Carbon
FTIR Data: Inorg./Org. SEI Components
Consumption of Li

Figure 15 .